

Article

High-Temperature Compression Behaviors and Constitutive Models of a 7046-Aluminum Alloy

Daoguang He ^{1,2,*} , Han Xie ^{1,2}, Yongcheng Lin ^{1,2} , Zhengbing Xu ³, Xianhua Tan ^{1,2,*} and Gang Xiao ¹

¹ School of Mechanical and Electrical Engineering, Central South University, Changsha 410083, China; 213711034@csu.edu.cn (H.X.); yclin@csu.edu.cn (Y.L.); xg_hnu@163.com (G.X.)

² State Key Laboratory of Precision Manufacturing for Extreme Service Performance, Changsha 410083, China

³ Guangxi Key Laboratory of Processing for Non-Ferrous Metals and Featured Materials, Nanning 530004, China; 51happiness123@163.com

* Correspondence: daoguanghe@csu.edu.cn (D.H.); xianhuatan@csu.edu.cn (X.T.); Tel.: +86-015273177698 (D.H.)

Abstract: High-temperature forming behaviors of a 7046-aluminum alloy were investigated by hot compression experiments. The microstructural evolution features with the changes in deformation parameters were dissected. Results indicated the formation of massive dislocation clusters/cells and subgrains through the intense DRV mechanism at low compression temperature. With an increase in deformation temperature, the annihilation of dislocations and the coarsening of subgrains/DRX grains became prominent, due to the collaborative effects of the DRV and DRX mechanisms. However, the growth of subgrains and DRX grains displayed the weakening trend at high strain rates. Moreover, two constitutive models involving a physically based (PB) model and a gate recurrent unit (GRU) model were proposed for predicting the hot compression features. By validation analysis, the predicted values of true stress perfectly fit with the experimental data, indicating that both the proposed PB model and the GRU model can accurately predict the hot compression behaviors of 7046-aluminum alloys.

Keywords: high-temperature compression behaviors; 7046-aluminum alloys; constitutive models; microstructure evolution



Citation: He, D.; Xie, H.; Lin, Y.; Xu, Z.; Tan, X.; Xiao, G. High-Temperature Compression Behaviors and Constitutive Models of a 7046-Aluminum Alloy. *Materials* **2023**, *16*, 6412. <https://doi.org/10.3390/ma16196412>

Academic Editors: Balázs Illés and Tomasz Czujko

Received: 30 July 2023

Revised: 13 September 2023

Accepted: 22 September 2023

Published: 26 September 2023



Copyright: © 2023 by the authors. Licensee MDPI, Basel, Switzerland. This article is an open access article distributed under the terms and conditions of the Creative Commons Attribution (CC BY) license (<https://creativecommons.org/licenses/by/4.0/>).

1. Introduction

Aluminum alloys have attracted considerable attention for military aircraft, automobiles and weapons because of their preeminent mechanical properties and corrosion resistance [1–6]. Due to the addition of numerous alloying elements, the aluminum alloys are frequently subjected to various microstructural evolution mechanisms [7,8], which results in the appearance of complicated hot flow features [9–12]. Hence, further research into the flow characteristics and microstructural evolution features of aluminum alloys in hot deforming is essential.

Researchers have systematically investigated how these microstructure evolution characteristics were conducive to regulating the hot flow features of aluminum alloys [13–15]. First, the evolution of dislocations and the coarsening behaviors of subgrains were deeply revealed in numerous studies [16–18]. Moreover, the development features in dynamic recrystallization (DRX) grains and the extension of grain boundaries in aluminum alloys were researched [19–22]. In addition, the precipitation behaviors and the dissolution features of phase were dissected [23,24].

Recently, many constitutive models were established or improved to capture the hot tensile/compression flow features of alloys [25–31]. For instance, the evolution features of flow behaviors with the Zener–Hollomon (Z) parameters were explored, and various phenomenological equations were constructed for depicting hot deforming features in aluminum alloys [32–34]. Meanwhile, numerous physically based (PB) equations were

constructed to predict the hot flow stress and microstructures for aluminum alloys [35–38], Ni-based alloys [39] and ultrahigh-strength steels [40,41]. In addition, various artificial neural network (ANN) models [42–44] containing BP models [45–47] and long short-term memory (LSTM) models [48,49] have been used to predict hot flow behaviors in aluminum alloys. Another preferred LSTM model, called a gate recurrent unit (GRU) neural network, was developed from ANN models. The GRU model contains fewer parameters than the LSTM model, thus boosting its computing efficiency while simultaneously improving the prediction accuracy [50,51]. Nowadays, as GRU theory continues to advance, GRU models are extensively used in various domains, including data modeling [52], text classification [53] and electric power load forecasting [54].

Although numerous investigations have focused on exploring hot deforming behaviors in aluminum alloys, the complicated microstructure evolution mechanisms and hot flow behaviors need to be further explored. In this investigation, the evolution characteristics of true stress and microstructures for the 7046-aluminum alloy are explored. Especially, the evolution features of dislocation clusters/subgrains and DRX nucleating mechanisms are revealed. Additionally, both a PB model and a GRU model were set up for describing the hot compression stress–strain characteristics in the 7046-aluminum alloy. Simultaneously, the reconstitution capacity of each constitutive model was verified.

2. Materials and Experimental Approach

In the present investigation, a commercial 7046-aluminum alloy with the chemical components (wt.%) of 6.6Zn-1.7Mg-0.25Cu-0.15Zr-Al (Bal) was used. Normal cylindrical specimens ($\phi 8 \text{ mm} \times 12 \text{ mm}$) were fabricated from the 7046-aluminum alloy plate. Hot compression experiments were executed on a Gleeble-3500 device (Poestenkill, NY, USA). The details of the hot compression process are revealed in Figure 1. The specimens were heated to setting forming temperature (T) and then held 360 s. The hot compression of each sample was implemented at a constant value of T and strain rate ($\dot{\epsilon}$). The values of T were selected to be from 300 °C to 450 °C with intervals of 50 °C. Moreover, the values of $\dot{\epsilon}$ were set as 0.001–1 s^{−1}, and the final strain was 0.92. When the final strain was reached, the test specimens were quickly cooled by water.

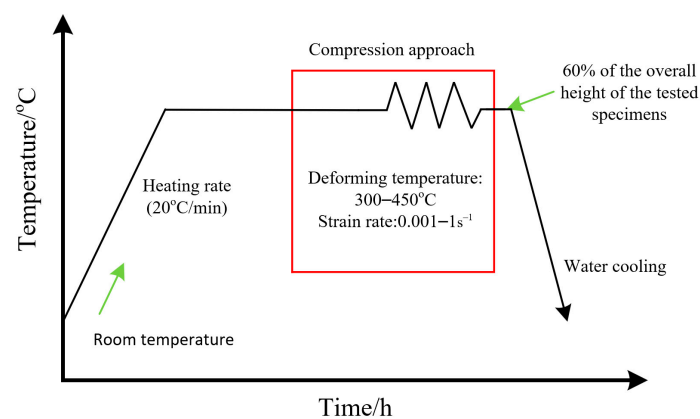


Figure 1. The hot forming steps for a 7046-aluminum alloy.

Backscattering electron microscopy (EBSD) (Velocity Super, EDAX-Ametek, Pleasanton, CA, USA) was utilized to examine the initial microstructure of the investigated 7046-aluminum alloy. In order to analyze the microstructural evolution features in hot compression, optical microscopy (OM) (Olympus DSX500, Tokyo, Japan) and a transmission electron microscope (TEM) (Tecnai G2 F20, FEI Company, USA) were used. Specimens for OM observations were first mechanically ground and polished, followed by etching with a Keller reagent [4]. For the TEM and EBSD observations, the pieces were mechanized along the axial direction of hot compressed samples and substantially polished in a solution (15 mL HClO₄ and 135 mL CH₃CH₂OH).

Figure 2 displays the EBSD images of the initial microstructure. Obviously, some equiaxed grains can be detected (Figure 2a). Moreover, almost all the grains are covered with the color blue, which demonstrates that few substructures remained (Figure 2b).

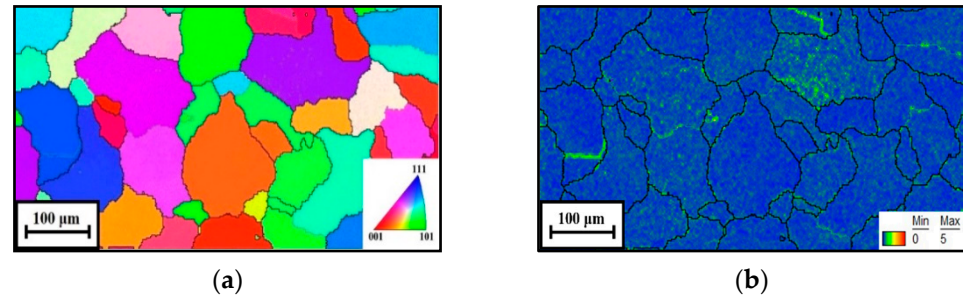


Figure 2. The EBSD analysis of the initial microstructure: (a) IPF image; (b) KAM image.

3. High-Temperature Compression Characteristics

3.1. Analysis of Hot Compression Flow Curves

Figure 3 reveals the flow behaviors of the 7046-aluminum alloy in hot compression. The similar evolution tendency in all the curves revealed that true stresses swiftly increase because of the acute work hardening (WH) effect correlated with the evolution of substructures [18]. When the hot compression continues, a decrease in true stress occurs due to the cooperation effects of the dynamic recovery (DRV) and dynamic recrystallization (DRX) [22]. Furthermore, it was revealed that true stresses are reduced with the decreasing strain rate ($\dot{\epsilon}$), as seen in Figure 3a. This is because an extended deformation time is provided to the development of subgrains and DRX grains with the decrease in $\dot{\epsilon}$. Thus, the softening effects associated with the mechanisms of DRV and DRX are enhanced, resulting in the decrease of true stresses. Moreover, the true stresses display the decreasing trend with the increase of deformation temperature (T), as seen in Figure 3b. One cause is that the DRV mechanism connected with the annihilation of dislocation clusters and the development of subgrains is improved at higher T . Moreover, the progression of DRX features also displays the reinforcing effect with the elevated T . Hence, the decrease of the true stress emerges.

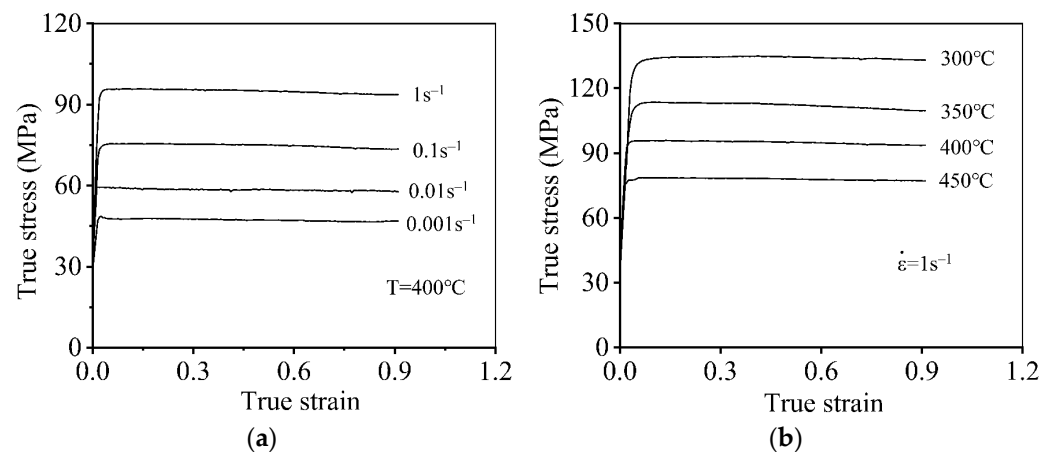


Figure 3. Typical hot-compressed features of the 7046-aluminum alloy at: (a) $T = 400\text{ }^{\circ}\text{C}$; (b) $\dot{\epsilon} = 1\text{ s}^{-1}$.

3.2. Microstructure Evolution Mechanisms

The typical evolution features of dislocations and subgrains with the variation of compressed parameters were explored by TEM observation (Figure 4). Clearly, some dislocations are generated and accumulated to form the dislocation networks/cells at $300\text{ }^{\circ}\text{C}/0.001\text{ s}^{-1}$, as seen in Figure 4a. Concurrently, many subgrains can also be observed. With the increase of T , the DRX grains become apparently coarsening and the annihilation of substructures are enhanced (Figure 4b). It is because that the diffusion of alloy

atoms/vacancies are sensibly reinforced at higher T [15], which enhances the consumption of substructures through the intense DRV mechanism. Furthermore, the expansion rate of grain boundaries is becoming strengthened with the increase of T [19], and then the coarsening capacity of DRX grains is significantly enhanced. With the $\dot{\epsilon}$ increasing to 1 s^{-1} , the nucleation of high-density substructures containing dislocation clusters/arrays and subgrains can be observed (Figure 4c). Simultaneously, almost all DRX grains at $400 \text{ }^\circ\text{C}/0.001 \text{ s}^{-1}$ become coarsening, compared to that seen at $400 \text{ }^\circ\text{C}/1 \text{ s}^{-1}$. The predominant cause is that the shorter deforming time for the dislocations' climbing/interaction and the propagation of grain boundaries can be ensured at higher $\dot{\epsilon}$ [29,39].

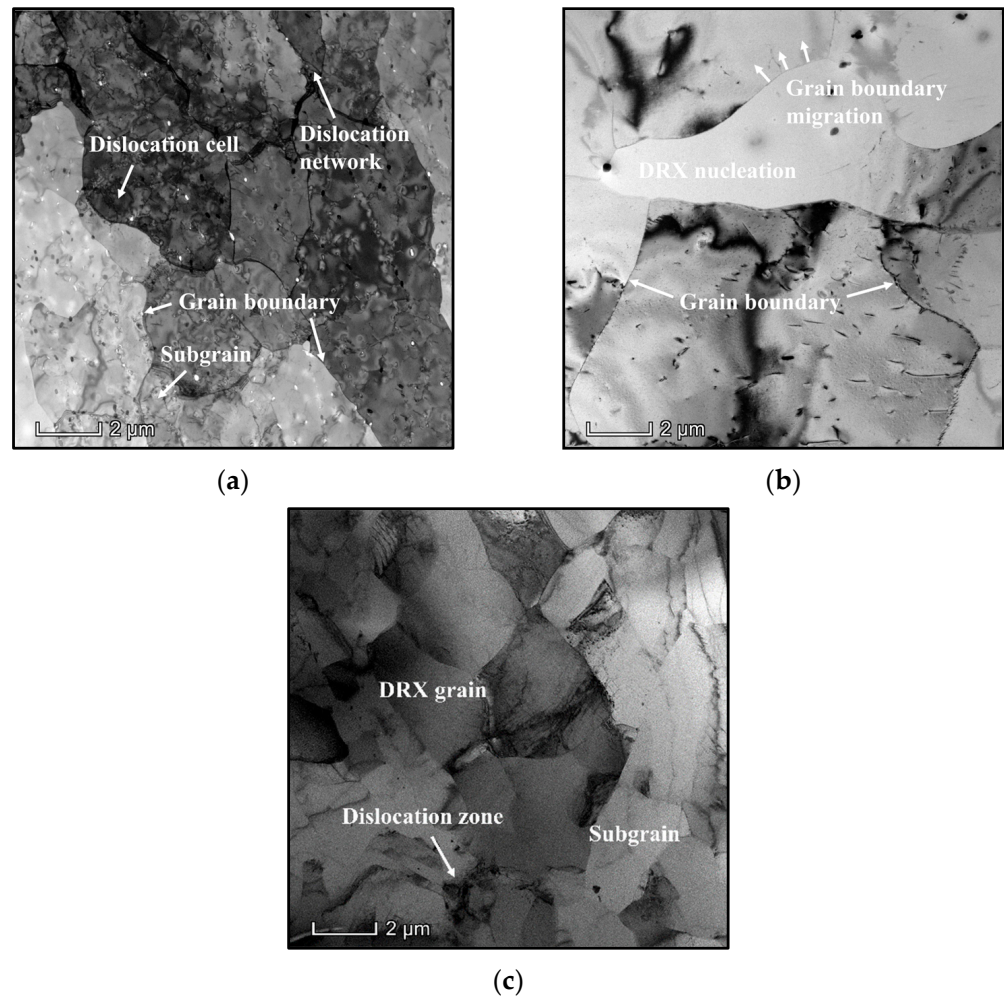


Figure 4. TEM maps at: (a) $300 \text{ }^\circ\text{C}/0.001 \text{ s}^{-1}$; (b) $400 \text{ }^\circ\text{C}/0.001 \text{ s}^{-1}$; (c) $400 \text{ }^\circ\text{C}/1 \text{ s}^{-1}$.

Figure 5 reveals the typical evolution features of grain morphology under different forming conditions. Clearly, the almost original grains reveal elongated characteristics at $400 \text{ }^\circ\text{C}/1 \text{ s}^{-1}$, and several fine DRX grains gather near them (Figure 5a). With the T increasing to $450 \text{ }^\circ\text{C}$, the nucleation and coarsening behaviors of DRX grains become apparent (Figure 5b). The main cause is that the significant development of substructures appears at high T , which promotes the formation of DRX nucleus. Meanwhile, the pinning effect for the grain boundaries becomes weakened due to the annihilation of high-density substructures, which is beneficial for DRX grain coarsening. Moreover, the DRX grains also display the coarsening tendency with the decrease of $\dot{\epsilon}$ (Figure 5c,d). That is because the deforming time for the consumption of substructures through the annihilation of dislocations and the diffusion of vacancies is extended, which reduces the resistance to the grain boundary migration. Thus, the DRX grains reflect the outstanding growth behaviors at lower $\dot{\epsilon}$.

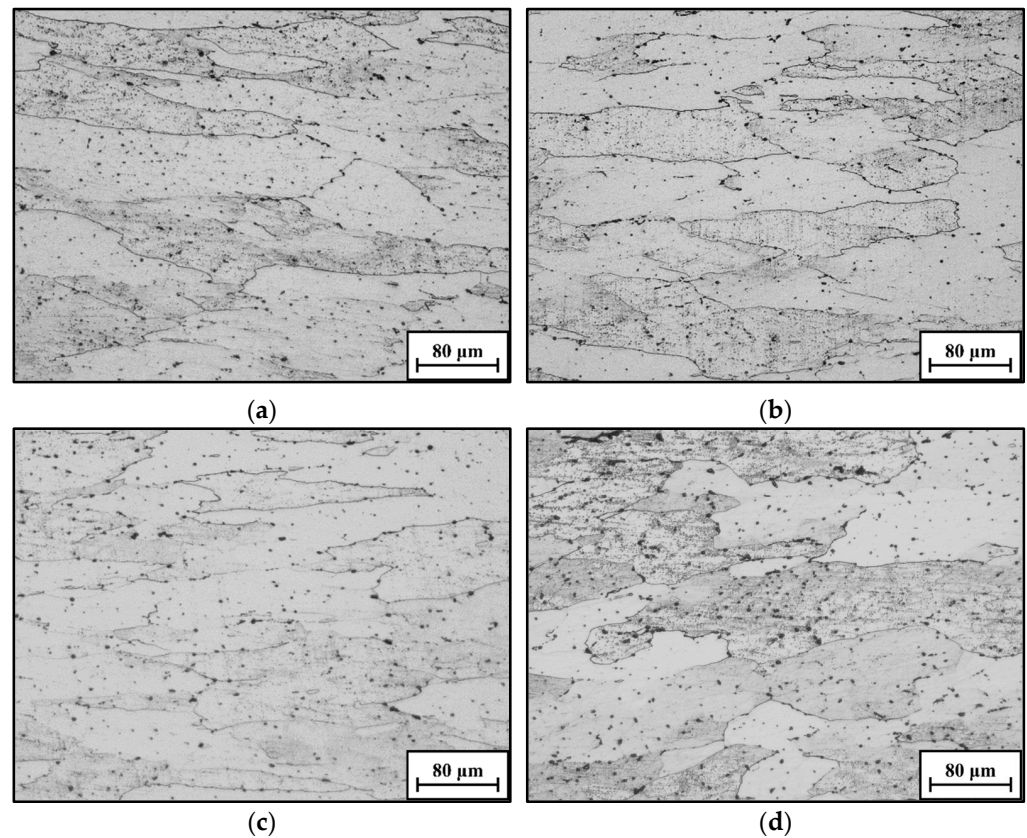


Figure 5. OM maps at: (a) 400 °C/1 s⁻¹; (b) 450 °C/1 s⁻¹; (c) 450 °C/0.01 s⁻¹; (d) 450 °C/0.001 s⁻¹.

4. Constitutive Models for Predicting High-Temperature Compression Behavior

4.1. A Proposed PB Model

4.1.1. Modeling the Flow Stress Induced by Work Hardening and Dynamic Recovery

Due to the interaction of WH and DRV mechanisms, the flow stress in the initial period of hot compression displays a sharply increasing tendency (Figure 3), and its evolution behavior can be described utilizing the Estrin–Mecking model [55],

$$\sigma_{\text{rec}} = \left[\sigma_{\text{sat}}^2 + \left(\sigma_y^2 - \sigma_{\text{sat}}^2 \right) \exp(-2\psi\epsilon) \right]^{1/2} \quad (1)$$

where σ_{rec} is flow stresses, σ_y is the yield stress, σ_{sat} is the saturation stress, ϵ is strain, and ψ is the material constant.

Commonly, the evolution characteristics of σ_y and σ_{sat} for alloys in hot deforming are tightly associated with the Zener–Hollomon (Z) parameter [55]. Accordingly, the Z parameter is usually ascertained as [32],

$$Z = \dot{\epsilon} \exp\left(\frac{Q}{RT}\right) \quad (2)$$

$$\dot{\epsilon} = \begin{cases} A[\sinh(\alpha\sigma)]^n \exp\left(-\frac{Q}{RT}\right), & \text{for all } \sigma \\ B\sigma^{n'} \exp\left(-\frac{Q}{RT}\right), & \alpha\sigma < 0.8 \\ C \exp(\beta\sigma) \exp\left(-\frac{Q}{RT}\right), & \alpha\sigma > 1.2 \end{cases} \quad (3)$$

where the Q is the deforming activated energy, R is the gas constant (8.314 J/mol/K), and A , B , C , n , n' and β are material constants.

The peak stress (σ_p) is commonly used to evaluate the material constants in n [56]. The σ_p is substituted into Equation (3) and it is given as [57],

$$\begin{cases} \dot{\epsilon} = B'\sigma_p^{n'}, \alpha\sigma_p < 0.8 \\ \dot{\epsilon} = C' \exp(\beta\sigma_p), \alpha\sigma_p > 1.2 \end{cases} \quad (4)$$

where B' and C' are material constants.

According to Equation (4), the values of n' and β are identified by the correlations of $\ln \dot{\epsilon} - \ln \sigma_p$ and $\ln \dot{\epsilon} - \sigma_p$, respectively. For the researched 7046-aluminum alloy, the variation characteristics of $\ln \dot{\epsilon} - \ln \sigma_p$ and $\ln \dot{\epsilon} - \sigma_p$ are revealed in Figure 6. Then, the mean values of n' and β are identified as 11.239 and 0.146, respectively. Accordingly, the $\alpha = \beta/n' = 0.0130 \text{ MPa}^{-1}$.

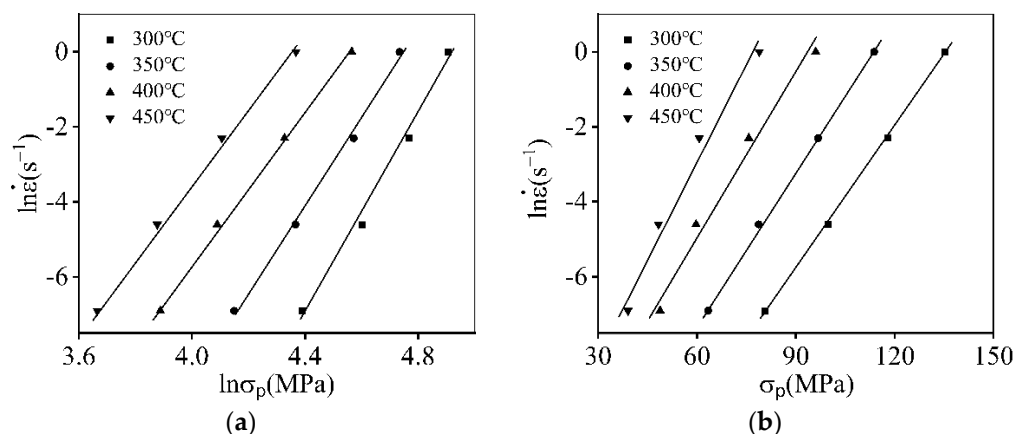


Figure 6. The plots of: (a) $\ln \dot{\epsilon} - \ln \sigma_p$; (b) $\ln \dot{\epsilon} - \sigma_p$.

Moreover, the Q in Equation (3) is identified by [58],

$$Q = R \left\{ \frac{\partial \ln \dot{\epsilon}}{\partial \ln [\sinh(\alpha\sigma_p)]} \right\}_T \cdot \left\{ \frac{\partial \ln [\sinh(\alpha\sigma_p)]}{\partial (1/T)} \right\}_{\dot{\epsilon}} \quad (5)$$

Figure 7 reveals the variation characteristics of $\ln \dot{\epsilon} - \ln [\sinh(\alpha\sigma_p)]$ and $\ln [\sinh(\alpha\sigma_p)] - 1/T$. Through the linear-fitting computation, the Q is estimated as 170.260 kJ/mol, which is similar to that of other Al-Zn-Mg-Cu alloys [27].

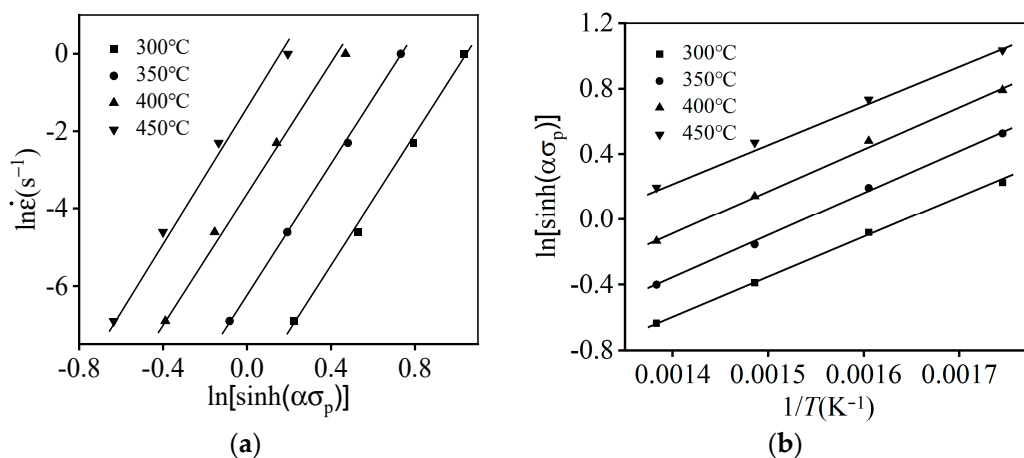


Figure 7. Correlations of: (a) $\ln \dot{\epsilon} - \ln [\sinh(\alpha\sigma_p)]$; (b) $\ln [\sinh(\alpha\sigma_p)] - 1/T$.

In addition, the values of σ_{sat} for alloys in hot deforming are usually determined by the $\theta = d\sigma/d\epsilon$ and σ curve [59]. Figure 8 reveals the variations in σ_{sat} and σ_y with the Z

parameters. As revealed in Figure 8a, the correlation of σ_{sat} and $\ln Z$ exhibits nonlinear characteristics. Concurrently, the evolution characteristics of σ_y over the Z parameter are revealed in Figure 8b. Based on the polynomial fitting method, the variations in σ_{sat} and σ_y with $\ln Z$ are identified, respectively, as listed in Equations (6) and (7).

$$\sigma_{sat} = 369.837 - 41.726 \ln Z + 1.595(\ln Z)^2 - 0.017(\ln Z)^3 \tag{6}$$

$$\sigma_y = 422.452 - 59.247 \ln Z + 2.244(\ln Z)^2 - 0.027(\ln Z)^3 \tag{7}$$

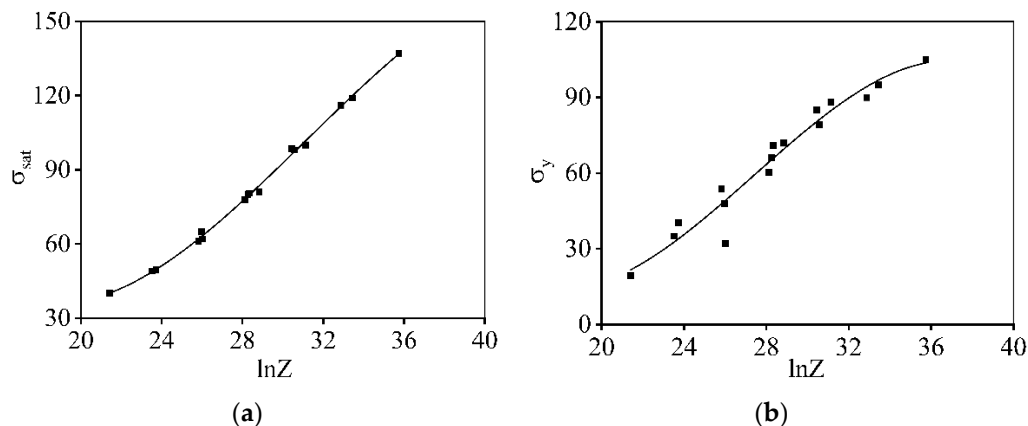


Figure 8. Relation of: (a) $\sigma_{sat} - \ln Z$, (b) $\sigma_y - \ln Z$.

Furthermore, the material constant of ψ in Equation (1) can be determined by

$$\psi = \frac{1}{2\epsilon} \ln \left(\frac{\sigma_{sat}^2 - \sigma_y^2}{\sigma_{sat}^2 - \sigma_{rec}^2} \right) \tag{8}$$

Using the experimental data, the relations of $\ln \psi$ and $\ln Z$ can be determined, as revealed in Figure 9. Clearly, the variation feature of $\ln \psi$ and $\ln Z$ displays the linear correlation. Hence, the ψ is identified as

$$\psi = 1998.2Z^{-0.164} \tag{9}$$

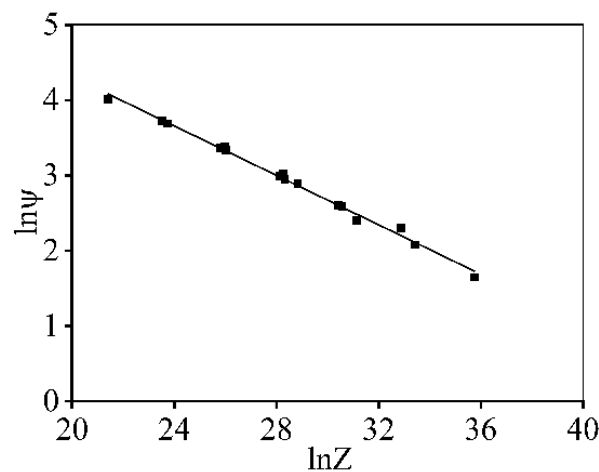


Figure 9. Relation between ψ and $\ln Z$.

4.1.2. Modeling the Flow Stress Induced by Work Hardening and DRX

As the DRX is excited, the flow stress descends notably due to the mutual influences of DRX and DRV [22]. Normally, the DRX fraction (X) is identified as [60],

$$X = \frac{\sigma_{\text{rec}} - \sigma_{\text{drx}}}{\sigma_{\text{sat}} - \sigma_{\text{ss}}} \quad (10)$$

where σ_{ss} is steady-state stress.

Moreover, the X is intimately influenced by the critical strain (ε_c) and can be identified as [60],

$$X = 1 - \exp[-c_1(\varepsilon - \varepsilon_c)^{c_2}] \quad (11)$$

where c_1 and c_2 are material constants.

Using Equations (1) and (11), the σ_{drx} is determined as [55],

$$\sigma_{\text{drx}} = \sigma_{\text{rec}} - \{1 - \exp[-c_1(\varepsilon - \varepsilon_c)^{c_2}]\}(\sigma_{\text{rec}} - \sigma_{\text{ss}}), \varepsilon \geq \varepsilon_c \quad (12)$$

Clearly, the values of σ_{drx} are primarily associated with the four factors ($c_1, c_2, \varepsilon_c, \sigma_{\text{ss}}$). Figure 10 reveals the variations in σ_{ss} with the Z parameters. Using the polynomial fitting analysis, the σ_{ss} can be ascertained as

$$\sigma_{\text{ss}} = 626.56 - 68.729 \ln Z + 2.542(\ln Z)^2 - 0.029(\ln Z)^3 \quad (13)$$

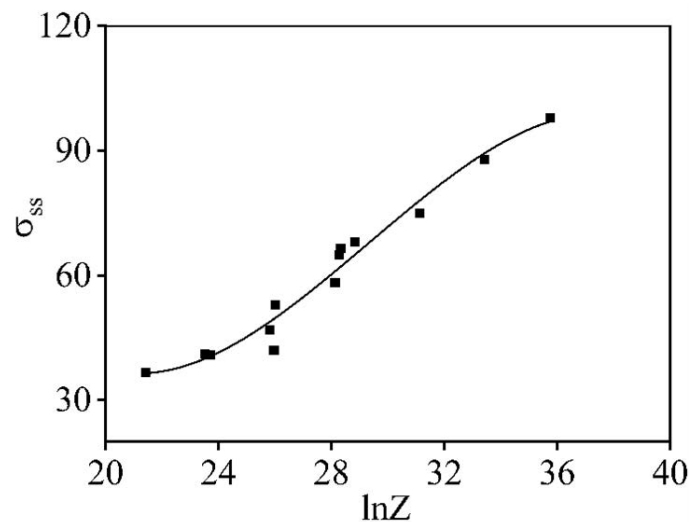


Figure 10. Relation between σ_{ss} and $\ln Z$.

In addition, for alloys in hot deforming, the correlation between ε_c and peak strain (ε_p) is commonly identified as [61],

$$\varepsilon_c = S_c \varepsilon_p \quad (14)$$

where S_c is the material constant. For Al-Zn-Mg-Cu alloys in hot deforming, the scopes of S_c are often chosen as 0.6~0.8 [61]. Here, the value of S_c is selected as 0.8.

Figure 11 reveals the changes of ε_p with Z parameters. Using the linear-fitting calculation, the ε_p is determined as

$$\varepsilon_p = 44.964Z^{5.462} \quad (15)$$

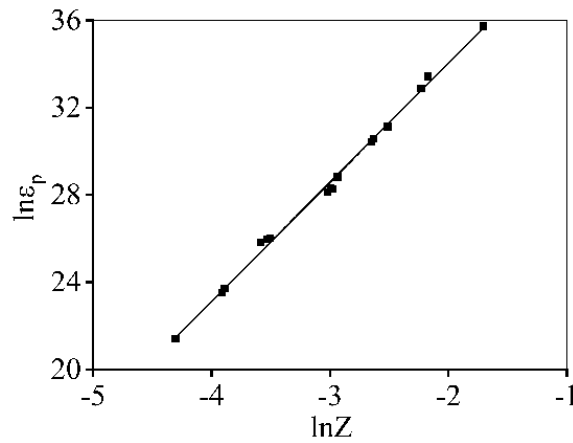


Figure 11. Relation between $\ln \epsilon_p$ and $\ln Z$.

Based on Equation (11), the values of two material constants (c_1 and c_2) can be identified utilizing linear regression analysis of the $\ln(-\ln(1 - X)) - \ln(\epsilon - \epsilon_c)$ plots. The changes of the material constants (c_1 and c_2) with the Z parameters are indicated in Figure 12a,b. Then, c_1 and c_2 can be determined as

$$c_1 = 36.162Z^{-0.179} \tag{16}$$

$$c_2 = 0.078Z^{0.068} \tag{17}$$

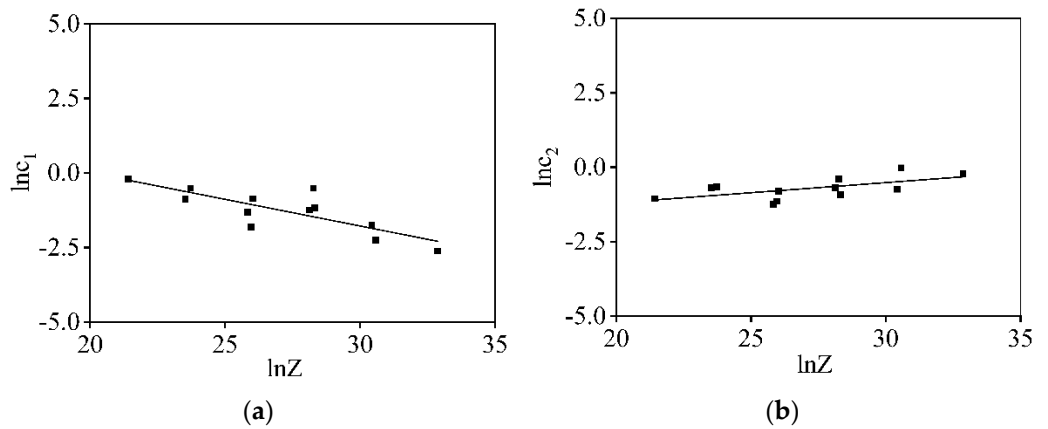


Figure 12. Relations of: (a) $\ln c_1 - \ln Z$; (b) $\ln c_2 - \ln Z$.

According to the above analysis, the constituted PB model can be summarized as

$$\left\{ \begin{array}{l} \sigma_{rec} = \left[\sigma_{sat}^2 + (\sigma_y^2 - \sigma_{sat}^2) \exp(-2\psi\epsilon) \right]^{1/2} \\ \sigma = \sigma_{rec} - \{1 - \exp[-c_1(\epsilon - \epsilon_c)^{c_2}]\} (\sigma_{rec} - \sigma_{ss}), \epsilon \geq \epsilon_c \\ \sigma_{sat} = 369.837 - 41.726 \ln Z + 1.595(\ln Z)^2 - 0.017(\ln Z)^3 \\ \sigma_y = 422.452 - 59.247 \ln Z + 2.244(\ln Z)^2 - 0.027(\ln Z)^3 \\ \sigma_{ss} = 626.56 - 68.729 \ln Z + 2.542(\ln Z)^2 - 0.029(\ln Z)^3 \\ \psi = 1998.2Z^{-0.164} \\ c_1 = 36.162Z^{-0.179} \\ c_2 = 0.078Z^{0.068} \\ Z = \dot{\epsilon} \exp\left(\frac{170260}{RT}\right) \\ \epsilon_p = 44.964Z^{5.462} \\ \epsilon_c = 0.8\epsilon_p \end{array} \right. \tag{18}$$

In addition, the values of the material constants in Equation (18) are listed in Table 1.

Table 1. The material constants of the 7046-aluminum alloy.

| Number | Notation | Values | Note |
|--------|----------------|--------------------------|----------------------------|
| 1 | Q | 170.260 kJ/mol | deforming activated energy |
| 2 | R | 8.314 J/mol/K | gas constant |
| 3 | n' | 11.239 | material constant |
| 4 | β | 0.146 | material constant |
| 5 | α | 0.0130 MPa ⁻¹ | material constant |
| 6 | S _c | 0.8 | material constant |

4.2. The GRU Machine Learning Model

As analyzed in Section 3.1, the changes in true stress with forming parameters ($T, \dot{\epsilon}$ and ϵ) indicate the typical nonlinear characteristics. Due to its superior data-driven performance for modeling multi-factor coupled data, a GRU model was proposed to capture the hot compression features of the researched aluminum alloy.

Figure 13 depicts the typical architecture of the GRU model. Commonly, the GRU model can dynamically update the implied state of the following cell in real time based on the historical data of the preceding GRU cell. Generally, the cyclic essence of the GRU model is reflected in the fact that model inputs (x_t) and the previous output hidden state (y_{t-1}) are transferred to the next GRU cell. Hot compression parameters containing $T, \dot{\epsilon}$ and ϵ are introduced to the network structure as the inputs, and the calculated results of the GRU cells are σ .

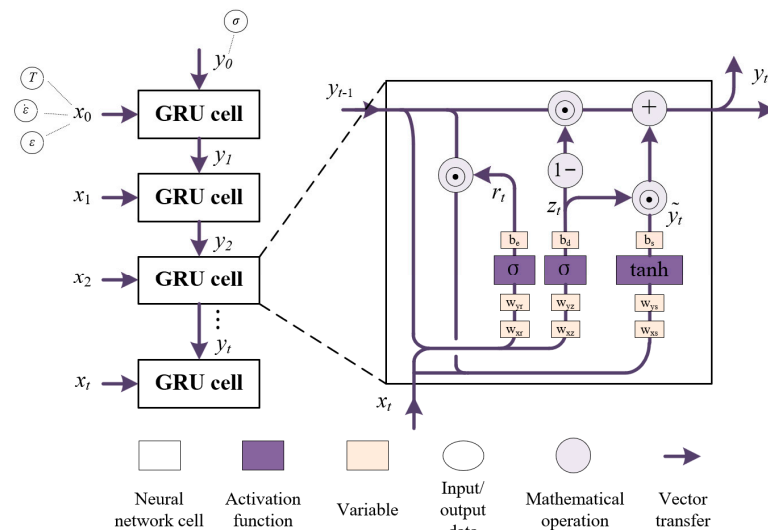


Figure 13. Schematic diagram of GRU cells.

Normally, GRU cells internally incorporate sophisticated and flexible structures, called gate connections, as shown in Figure 13. The gate connections, predominantly both reset gates (r_t) and update gates (z_t), are responsible for the learning and computational processes of the input data in the GRU model.

Primarily, the reset gates (r_t) regulate how much state information from the previous state will be ignored in the hidden layer vector [52].

Normally, the equation of r_t can be expressed as [52],

$$r_t = \sigma(W_{xr}x_t + W_{yr}y_{t-1} + b_r) \tag{19}$$

where W_{xr} and W_{yr} are neuron connection weights of the reset gate, b_e is the bias of the reset gate, and $\sigma(t)$ is the sigmoid activation function, which can be indicated as

$$\sigma(t) = \frac{1}{1 + e^{-t}} \quad (20)$$

where t indicates input elements.

Next, the update gate (z_t) modulates how much state information from the previous implicit layer is maintained to the candidate hidden state. The update gate (z_t) can be expressed as [51],

$$z_t = \sigma(W_{xz}x_t + W_{yz}y_{t-1} + b_d) \quad (21)$$

where W_{xz} and W_{yz} are neuron connection weights of the update gate, and b_d is the bias of the update gate.

The candidate hidden state (\tilde{y}_t) contains the most recent time step information, and can be updated as follows [50]:

$$\tilde{y}_t = \tanh(W_{xs} \cdot x_t + W_{ys} \cdot (r_t \odot y_{t-1}) + b_s) \quad (22)$$

where the symbol \odot is multiplication of elements. $\tanh(t)$ is the hyperbolic tangent function, which can be represented as

$$\tanh(t) = \frac{e^t - e^{-t}}{e^t + e^{-t}} \quad (23)$$

In conclusion, the final update gets the hidden state of the current time step and can be expressed as [53],

$$y_t = (1 - z_t) \odot y_{t-1} + z_t \odot \tilde{y}_t \quad (24)$$

Prior to training the GRU model, the input data is normalized and the normalization expression can be revealed as

$$X'_{in} = \frac{X_{in} - X_{in}^{(\min)}}{X_{in}^{(\max)} - X_{in}^{(\min)}} \quad (25)$$

where X'_{in} is the normalized data, X_{in} is the original data, and $X_{in}^{(\max)}$ and $X_{in}^{(\min)}$ are the maximum and minimum values of X_{in} , respectively. After the normalization of input data, the corresponding values (T' , ϵ' , ϵ') are collapsed into sequences as training inputs. Here, the experimental data utilization was split at random into 80% for model training and the remaining 20% for model testing and validation.

Commonly, the excellent predictive accuracy and rapid response of the GRU model are impacted by the diverse hyperparameters. The numbers of hidden layers and neurons in the hidden layers, the initial learning rate and the batch size are the main alterable hyperparameters of the GRU model. Various hidden layers can promote model accuracy, but it has been demonstrated that too many hidden layers will lead to overfitting [51]. In this paper, the number of hidden layers was set to three, balancing accuracy and overfitting. Additionally, the number of neurons in the hidden layers was set to decrease layer by layer. The learning rate and the batch size of the GRU model play the critical roles [62]. A higher initial learning rate or batch size allows for quicker training but may lead to a less accurate and unstable training. For further probing the connection between the three hyperparameters and the forecast results, an orthogonal experiment table with three factors and four levels was devised, as shown in Table 2. Based on that orthogonal experiment table, the calculated results of $L_{16}(3^4)$ are shown in Table 3. Here, the model accuracy is assessed by the validation loss, which is characterized using the mean squared error (MSE). The MSE equation is,

$$\text{MSE} = \frac{1}{N} \sum_{i=1}^N (E_i - P_i)^2 \quad (26)$$

where N is the number of values, E_i is the experimental stress, and P_i is the predicted stress.

Table 2. Orthogonal experiment table.

| Levels | Alterable Hyperparameters | | |
|--------|---------------------------|------------|-------------------------------------|
| | Initial Learning Rate | Batch Size | Numbers of Neurons in Hidden Layers |
| Case1 | 0.0001 | 8 | 120/100/80 |
| Case2 | 0.001 | 16 | 100/80/60 |
| Case3 | 0.01 | 32 | 80/60/40 |
| Case4 | 0.1 | 64 | 60/40/20 |

Table 3. Results of orthogonal devised list.

| Experimental Serial Number | Alterable Hyperparameters | | | MSE | Computing Time(s) |
|----------------------------|---------------------------|------------|-------------------------------------|--------|-------------------|
| | Initial Learning Rate | Batch Size | Numbers of Neurons in Hidden Layers | | |
| 1 | 0.0001 | 8 | 120/100/80 | 6.404 | 486.50 |
| 2 | 0.0001 | 16 | 100/80/60 | 9.975 | 246.07 |
| 3 | 0.0001 | 32 | 80/60/40 | 11.514 | 115.57 |
| 4 | 0.0001 | 64 | 60/40/20 | 13.563 | 75.64 |
| 5 | 0.001 | 8 | 100/80/60 | 2.279 | 434.68 |
| 6 | 0.001 | 16 | 120/100/80 | 6.227 | 274.20 |
| 7 | 0.001 | 32 | 60/40/20 | 6.829 | 110.30 |
| 8 | 0.001 | 64 | 80/60/40 | 6.406 | 286.22 |
| 9 | 0.01 | 8 | 80/60/40 | 2.798 | 496.59 |
| 10 | 0.01 | 16 | 60/40/20 | 3.151 | 237.23 |
| 11 | 0.01 | 32 | 120/100/80 | 2.254 | 263.03 |
| 12 | 0.01 | 64 | 100/80/60 | 1.955 | 124.73 |
| 13 | 0.1 | 8 | 60/40/20 | 32.259 | 458.46 |
| 14 | 0.1 | 16 | 80/60/40 | 52.799 | 217.19 |
| 15 | 0.1 | 32 | 100/80/60 | 44.525 | 149.15 |
| 16 | 0.1 | 64 | 120/100/80 | 45.622 | 139.82 |

Figure 14 describes the variations of MSE and computing time under different hyperparameters. On the one hand, the MSE of the GRU model decreases to a minimal value when the initial learning rate increases from 0.001 to 0.01. On the other hand, the MSE value begins to violently fluctuate as the initial learning rate ascends or declines; thus, the perfect learning rate can be set at 0.01. Meanwhile, as the batch size increases, the computation time can be effectively reduced without affecting the accuracy of the GRU model. Hence, the batch size was determined as 64. Summarily, the values of the initial learn rate, batch size and numbers of neurons in hidden layers were selected as 0.01, 64 and 100/80/60, respectively.

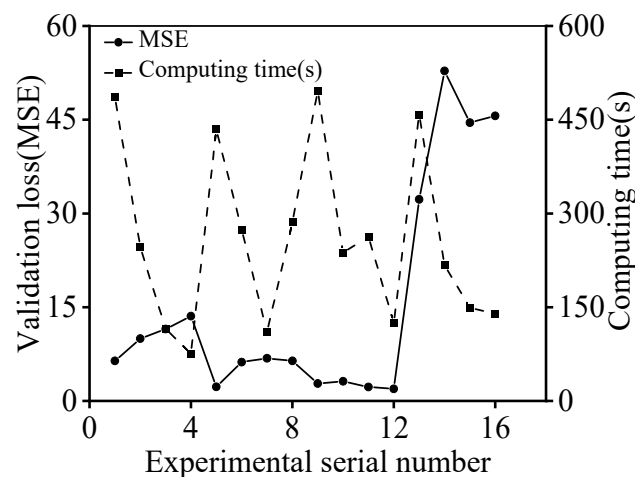


Figure 14. Variations in MSE and computing time under different hyperparameters.

4.3. Comparison and Validation

Based on the proposed PB and GRU models, the hot compression stress–strain features for the 7046-aluminum alloy are reconstituted. Figure 15 depicts the comparison analysis of the flow stress predicting ability of the proposed PB and GRU models. Clearly, the tested hot compression stresses match very well with the values predicted by the GRU model. The primary reason was that the GRU model has an outstanding ability to describe nonlinear correlations between input values and output results [54]. Moreover, a disparity between the tested compression stresses and the predicted ones utilized by the PB model was discovered at 300 °C (Figure 15a). However, the compression stresses preeminently fit the forecasting results as the T reached 350 °C or above (Figure 15c,d). The primary reason for these phenomena was that the microstructural evolution mechanisms are intimately connected with the compression parameters [23]. The DRV behavior acts as the predominant softening mechanism in the hot deforming process of a 7046-aluminum alloy when the T is less than 350 °C. Nevertheless, the DRX characteristics are activated when the T reaches 350 °C or above, and they evolve into the predominant softening mechanism for the 7046-aluminum alloy. Because of the appearance of varying microstructural evolution mechanisms, the variations in compression stresses over deforming parameters exhibit complicated and non-linear features. Thus, the forecasting accuracy of the PB model is relatively lower than that of the GRU model.

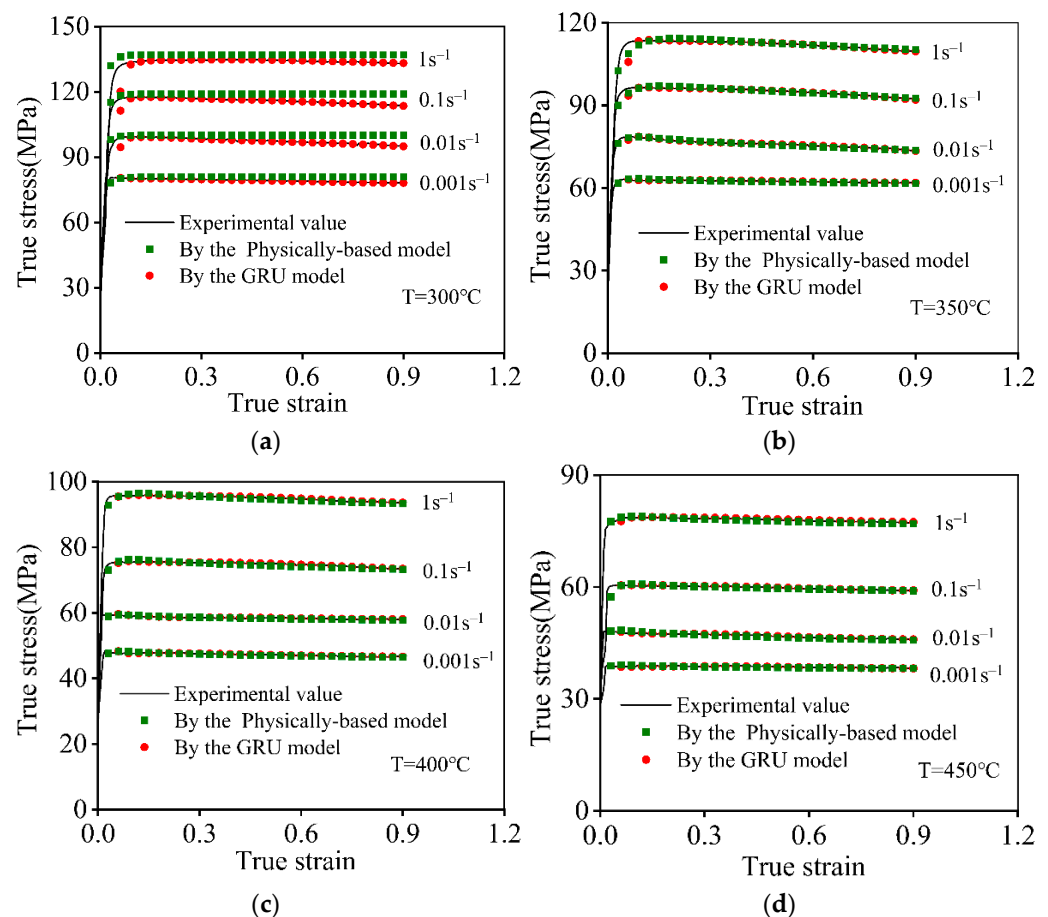


Figure 15. Comparative analysis of the tested stresses and the forecasted results at: (a) 300 °C; (b) 350 °C; (c) 400 °C; (d) 450 °C.

In addition, the average absolute relative error (AARE) and the correlation coefficient (C_C) were calculated to further estimate the forecasting ability of the PB model and the GRU model. The values of AARE and C_C are determined as

$$\text{AARE}(\%) = \frac{1}{N} \sum_{i=1}^N \left| \frac{E_i - P_i}{E_i} \right| \times 100\% \quad (27)$$

$$C_C = \frac{\sum_{i=1}^N (E_i - \bar{E})(P_i - \bar{P})}{\sqrt{\sum_{i=1}^N (E_i - \bar{E})^2 \sum_{i=1}^N (P_i - \bar{P})^2}} \quad (28)$$

where N is the number of the data; E_i and P_i are the testing stresses and forecasting ones, respectively; and \bar{E} and \bar{P} are the mean values of E_i and P_i , respectively.

The further correlation analyses of the tested stresses and the results forecast by the constructed PB and GRU models are shown in Figure 16. The values of the AARE for the PB model and the GRU model are determined to be 4.681% and 2.065%, respectively, which are less than 5.0%. Concurrently, the C_C values for the PB model and the GRU model are determined as 0.9989 and 0.9996, respectively. The relatively small AARE and large C_C show that both the PB model and the GRU model enjoy sufficient precision to capture the hot compression characteristics. Additionally, it can also be inferred that the proposed GRU model possesses better forecasting ability for the hot compression behaviors of a 7046-aluminum alloy than that of the PB model.

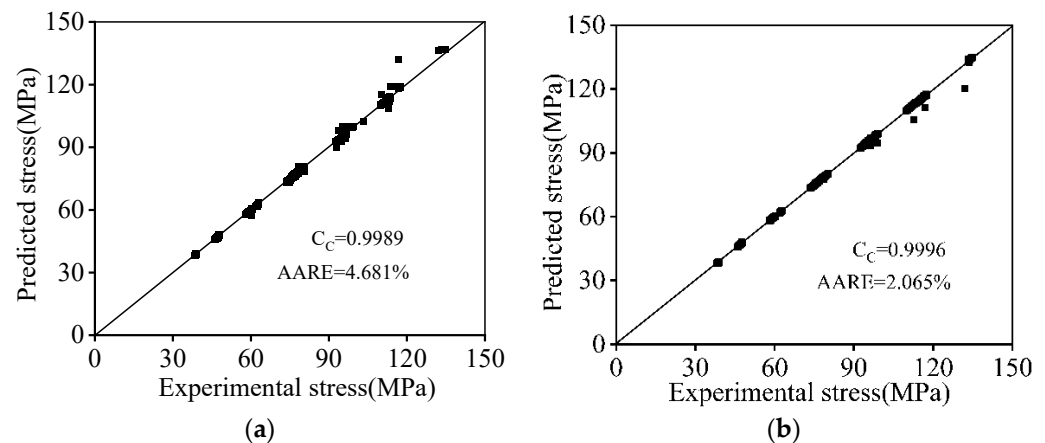


Figure 16. Relationships of tested compression stresses and values forecasted by (a) the PB model; (b) the GRU model.

Similar research on the hot tensile characteristics of the 7046-aluminum alloy can be found in the authors' previous study [48]. An improved Hensel–Spittel–Carofalo (HSC) model and a long short-term memory (LSTM) model are established to reconstruct the high-temperature tensile features. The C_C and AARE values of all four models are listed in Table 4. Comparing the four constitutive models, it is clear that the ANN models, including the LSTM model and the GRU model, had better forecast performance than the PB model and the HSC model. However, the PB model has the superior capability for predicting the hot forming behaviors for the 7046-aluminum alloy.

Table 4. The evaluation indicators of constitutive models.

| Constitutive Model | Evaluation Indicators | |
|-------------------------|-----------------------|--------|
| | C_C | AARE |
| PB model | 0.9989 | 4.681% |
| GRU model | 0.9996 | 2.065% |
| Improved HSC model [48] | 0.989 | 4.58% |
| LSTM model [48] | 0.998 | 2.16% |

5. Conclusions

Hot compression characteristics and microstructural evolution mechanisms for the 7046-aluminum alloy were revealed. Some prominent conclusions of this study are as follows:

- (1) Hot flow characteristics of a 7046-aluminum alloy are intimately associated with compression parameters. As compression temperature ascends or the strain rate descends, the flow stresses display the dominant reducing characteristic.
- (2) Microstructural evolution characteristics are intensely influenced by the compression parameters. The formation/interaction of substructures exhibits the intensified trend, while the extension of DRX grain boundaries becomes inhibited at a high strain rate or low compression temperature.
- (3) A PB model and a GRU model were proposed to describe the hot compression behaviors of the 7046-aluminum alloy. The relatively smaller AARE and larger C_C demonstrated that both the proposed PB model and the GRU model can precisely achieve the reconstitution of hot compression behaviors in the 7046-aluminum alloy.

Author Contributions: Conceptualization, D.H.; Methodology, H.X., Y.L. and X.T.; Validation, Z.X. and G.X.; Writing—original draft, D.H. and H.X.; Writing—review & editing, D.H. and Y.L.; Data curation, H.X. and Z.X.; Funding acquisition, D.H. and Y.L.; Software, H.X.; Investigation, H.X. and Z.X. All authors have read and agreed to the published version of the manuscript.

Funding: This work was supported by the National Natural Science Foundation of China (Grant No. 52005519, 52075159), the National Key Research and Development Program of China (No. 2022YFB3706902), the Hunan Provincial Natural Science Foundation of China (Grant Nos. 2021JJ40738, 2023JJ20065), the Changsha Municipal Natural Science Foundation (No. kq2007024), the State Key Laboratory of Featured Metal Materials and Life-cycle Safety for Composite Structures (2022GXYSOF04, 2022GXYSOF24), and the Postgraduate Scientific Research Innovation Project of Hunan Province (No. CX20220308).

Institutional Review Board Statement: Not applicable.

Informed Consent Statement: Not applicable.

Data Availability Statement: The raw/processed data acquired in present investigation cannot be shared at this time because the data also forms part of an ongoing research.

Conflicts of Interest: The authors declare no conflict of interest.

References

1. Yang, G.J.; Xu, W.C.; Jin, X.Z.; Wang, Z.Y.; Shan, D.B.; Guo, B. Hot deformation behavior and microstructure evolution of the spray deposited and secondary hot extruded 2195 Al–Li alloy. *J. Mater. Res. Technol.* **2022**, *20*, 2784–2798. [[CrossRef](#)]
2. Gupta, R.K.; Kumar, V.A.; Krishnan, A.S.; Niteshraj, J. Hot deformation behavior of aluminum alloys AA7010 and AA7075. *J. Mater. Eng. Perform.* **2019**, *28*, 5021–5036. [[CrossRef](#)]
3. Liu, J.; Jiang, F.L.; Tang, M.Z.; Liu, B.B.; Sun, Y.S.; Zhang, H. Reduced residual stress and retained properties in Al–Zn–Mg–Cu alloys using a novel cladding quenching process. *J. Mater. Res. Technol.* **2020**, *9*, 7201–7209. [[CrossRef](#)]
4. Chen, G.; Jiang, J.F.; Du, Z.M.; Han, F.; Atkinson, H.V. Hot tensile behavior of an extruded Al–Zn–Mg–Cu alloy in the solid and in the semi-solid state. *Mater. Des.* **2014**, *54*, 1–5. [[CrossRef](#)]
5. Azarniya, A.; Taheri, A.K.; Taheri, K.K. Recent advances in ageing of 7xxx series aluminum alloys: A physical metallurgy perspective. *J. Alloys Compd.* **2019**, *781*, 945–998. [[CrossRef](#)]

6. Chen, L.; Hou, Y.Z.; Li, Z.G.; Zhao, G.Q.; Zhang, C.S. Enhancing mechanical properties and corrosion resistance of a high strength 7A99 Al alloy by introducing pre-rolling in solution and aging treatments. *J. Alloys Compd.* **2022**, *898*, 162972. [[CrossRef](#)]
7. Quan, G.Z.; Shi, R.J.; Zhao, J.; Liu, Q.; Xiong, W.; Qiu, H.M. Modeling of dynamic recrystallization volume fraction evolution for AlCu4SiMg alloy and its application in FEM. *T. Nonferr. Metal. Soc.* **2019**, *29*, 1138–1151. [[CrossRef](#)]
8. Ren, X.W.; Huang, Y.C.; Liu, Y.; Zhao, Y.X.; Li, H. Evolution of microstructure, texture, and mechanical properties in a twin-roll cast AA6016 sheet after asymmetric rolling with various velocity ratios between top and bottom rolls. *Mater. Sci. Eng. A* **2020**, *788*, 139448. [[CrossRef](#)]
9. Zhao, J.H.; Deng, Y.L.; Tang, J.G.; Zhang, J. Influence of strain rate on hot deformation behavior and recrystallization behavior under isothermal compression of Al-Zn-Mg-Cu alloy. *J. Alloys Compd.* **2019**, *809*, 151788. [[CrossRef](#)]
10. Sun, Y.W.; Pan, Q.L.; Huang, Z.Q.; Wang, W.Y.; Wang, X.D.; Li, M.J.; Lai, J.P. Evolutions of diffusion activation energy and Zener-Hollomon parameter of ultra-high strength Al-Zn-Mg-Cu-Zr alloy during hot compression. *Prog. Nat. Sci. Mater. Int.* **2018**, *28*, 635–646. [[CrossRef](#)]
11. Zhang, Y.; Jiang, J.F.; Wang, Y.; Liu, Y.Z.; Huang, M.J. Hot deformation behavior and microstructure evolution of hot-extruded 6A02 aluminum alloy. *Mater. Charact.* **2022**, *188*, 111908. [[CrossRef](#)]
12. Chen, S.F.; Li, D.Y.; Zhang, S.H.; Han, H.N.; Lee, H.W.; Lee, M.G. Modelling continuous dynamic recrystallization of aluminum alloys based on the polycrystal plasticity approach. *Int. J. Plast.* **2020**, *131*, 102710. [[CrossRef](#)]
13. Ding, S.; Khan, S.A.; Yanagimoto, J. Flow behavior and dynamic recrystallization mechanism of A5083 aluminum alloys with different initial microstructures during hot compression. *Mater. Sci. Eng. A* **2020**, *787*, 139522. [[CrossRef](#)]
14. Li, J.C.; Wu, X.D.; Cao, L.F.; Liao, B.; Wang, Y.C.; Liu, Q. Hot deformation and dynamic recrystallization in Al-Mg-Si alloy. *Mater. Charact.* **2021**, *173*, 110976. [[CrossRef](#)]
15. Chen, G.; Zhang, Y.M.; Du, Z.M. Mechanical behavior of Al-Zn-Mg-Cu alloy under tension in semi-solid state. *Trans. Nonferrous Met. Soc. China* **2016**, *26*, 634–648. [[CrossRef](#)]
16. Feng, D.; Zhang, X.M.; Liu, S.D.; Deng, Y.L. Constitutive equation and hot deformation behavior of homogenized Al-7.68Zn-2.12Mg-1.98Cu-0.12Zr alloy during compression at elevated temperature. *Mater. Sci. Eng. A* **2014**, *608*, 63–72. [[CrossRef](#)]
17. Khan, M.A.; Wang, Y.W.; Hamza, M.; Yasin, G.; Tabish, M.; Feng, C.S.; Khan, W.Q.; Ahmad, T.; Liao, W.B.; Afifi, M.A. Precipitation behaviour in an Al-Zn-Mg-Cu alloy subjected to high strain rate compression tests. *Mater. Charact.* **2021**, *180*, 111398. [[CrossRef](#)]
18. Jiang, F.L.; Zhang, H.; Weng, S.C.; Fu, D.F. Characterization of dynamic microstructural evolution of AA7150 aluminum alloy at high strain rate during hot deformation. *T. Nonferr. Metal. Soc.* **2016**, *26*, 51–62. [[CrossRef](#)]
19. Sun, Y.W.; Pan, Q.L.; Wang, W.Y.; Li, A.D.; Song, W.B. Microstructural evolution and constitutive analysis combined with weight optimization method of Al-7.82Zn-1.96Mg-2.35Cu-0.11Zr alloy during hot deformation. *J. Alloys Compd.* **2018**, *732*, 902–914. [[CrossRef](#)]
20. Xu, C.C.; He, H.; Xue, Z.G.; Li, L.X. A detailed investigation on the grain structure evolution of AA7005 aluminum alloy during hot deformation. *Mater. Charact.* **2021**, *171*, 110801. [[CrossRef](#)]
21. Xu, C.L.; Huang, J.W.; Jiang, F.Q.; Jiang, Y.G. Dynamic recrystallization and precipitation behavior of a novel Sc, Zr alloyed Al-Zn-Mg-Cu alloy during hot deformation. *Mater. Charact.* **2022**, *183*, 111629. [[CrossRef](#)]
22. Luo, L.; Liu, Z.Y.; Bai, S.; Zhao, J.G.; Zeng, D.P.; Wang, J.; Cao, J.; Hu, Y.C. Hot deformation behavior considering strain effects and recrystallization mechanism of an Al-Zn-Mg-Cu Alloy. *Materials* **2020**, *13*, 1743. [[CrossRef](#)] [[PubMed](#)]
23. Xu, C.L.; Huang, J.W.; Jiang, F.Q.; Jiang, Y.G. The effect of strain rates on the microstructure and the mechanical properties of an over-aged Al-Zn-Mg-Cu alloy. *Mater. Charact.* **2020**, *167*, 110472.
24. Tian, X.; Chen, F.; Jiang, J.N.; Wu, G.S.; Cui, Z.S.; Qian, D.S.; Han, X.H.; Wang, B.; Wang, H.Q.; Wang, H. Experimental analyses and numerical modeling of the microstructure evolution of aluminum alloy using an internal state variable plasticity-based approach coupled with the effects of second phase. *Int. J. Plast.* **2022**, *158*, 103416. [[CrossRef](#)]
25. El Mehtedi, M.; Musharavati, F.; Spigarelli, S. Modelling of the flow behaviour of wrought aluminium alloys at elevated temperatures by a new constitutive equation. *Mater. Des.* **2014**, *54*, 869–873. [[CrossRef](#)]
26. Fakhar, N.; Khademi, E.; Momeni, A. High temperature behavior of severely deformed AA 5083 through equal channel lateral extrusion. *Mater. Chem. Phys.* **2020**, *243*, 122581. [[CrossRef](#)]
27. Zhou, M.; Lin, Y.C.; Deng, J.; Jiang, Y.Q. Hot tensile deformation behaviors and constitutive model of an Al-Zn-Mg-Cu alloy. *Mater. Des.* **2014**, *59*, 141–150. [[CrossRef](#)]
28. Zhang, D.N.; Shangguan, Q.Q.; Xie, C.J.; Liu, F. A modified Johnson-Cook model of dynamic tensile behaviors for 7075-T6 aluminum alloy. *J. Alloys Compd.* **2015**, *619*, 186–194. [[CrossRef](#)]
29. Savaedi, Z.; Motallebi, R.; Mirzadeh, H. A review of hot deformation behavior and constitutive models to predict flow stress of high-entropy alloys. *J. Alloys Compd.* **2022**, *903*, 163964. [[CrossRef](#)]
30. Su, Z.X.; Sun, C.Y.; Fu, M.W.; Qian, L.Y. Physical-based constitutive model considering the microstructure evolution during hot working of AZ80 magnesium alloy. *Adv. Manuf.* **2019**, *7*, 30–41. [[CrossRef](#)]
31. Lu, C.Y.; Shi, J.; Wang, J. Physically based constitutive modeling for Ti17 alloy with original basketweave microstructure in beta forging: A comparison of three approaches. *Mater. Charact.* **2021**, *181*, 111455. [[CrossRef](#)]
32. Chen, X.X.; Zhao, G.Q.; Zhao, X.T.; Wang, Y.X.; Xu, X.; Zhang, C.S. Constitutive modeling and microstructure characterization of 2196 Al-Li alloy in various hot deformation conditions. *J. Manuf. Process.* **2020**, *59*, 326–342. [[CrossRef](#)]

33. Ashtiani, H.R.R.; Shahsavari, P. Constitutive modeling of flow behavior of precipitation-hardened AA7022-T6 aluminum alloy at elevated temperature. *T. Nonferr. Metal. Soc.* **2020**, *30*, 2927–2940. [[CrossRef](#)]
34. Quan, G.Z.; Li, G.S.; Wang, Y.; Lv, W.Q.; Yu, C.T.; Zhou, J. A characterization for the flow behavior of as-extruded 7075 aluminum alloy by the improved Arrhenius model with variable parameters. *Mater. Res.-Ibero-AM J* **2013**, *16*, 19–27. [[CrossRef](#)]
35. Mirzadeh, H. Constitutive description of 7075 aluminum alloy during hot deformation by apparent and physically-based approaches. *J. Mater. Eng. Perform.* **2015**, *24*, 1095–1099. [[CrossRef](#)]
36. Zhang, H.M.; Chen, G.; Chen, Q.; Han, F.; Zhao, Z.D. A physically-based constitutive modelling of a high strength aluminum alloy at hot working conditions. *J. Alloys Compd.* **2018**, *743*, 283–293. [[CrossRef](#)]
37. Tang, J.; Jiang, F.L.; Luo, C.H.; Bo, G.W.; Chen, K.Y.; Teng, J.; Fu, D.F.; Zhang, H. Integrated physically based modeling for the multiple static softening mechanisms following multi-stage hot deformation in Al-Zn-Mg-Cu alloys. *Int. J. Plast.* **2020**, *134*, 102809. [[CrossRef](#)]
38. Liu, L.; Wu, Y.X.; Gong, H.; Li, S.; Ahmad, A.S. A physically based constitutive model and continuous dynamic recrystallization behavior analysis of 2219 aluminum alloy during hot deformation process. *Materials* **2018**, *11*, 1443. [[CrossRef](#)]
39. He, D.G.; Yan, X.T.; Lin, Y.C.; Zhang, S.; Chen, Z.J. Microstructure evolution and constitutive model for a Ni-Mo-Cr base alloy in double-stages hot compression with step-strain rates. *Mater. Charact.* **2022**, *194*, 112385. [[CrossRef](#)]
40. Wen, D.X.; Yue, T.Y.; Xiong, Y.B.; Wang, K.; Wang, J.K.; Zheng, Z.Z.; Li, J.J. High-temperature tensile characteristics and constitutive models of ultrahigh strength steel. *Mater. Sci. Eng. A* **2021**, *803*, 140491. [[CrossRef](#)]
41. Wen, D.X.; Gao, C.X.; Zheng, Z.Z.; Wang, K.; Xiong, Y.B.; Wang, J.K.; Li, J.J. Hot tensile behavior of a low-alloyed ultrahigh strength steel: Fracture mechanism and physically-based constitutive model. *J. Mater. Res. Technol.* **2021**, *13*, 1684–1697. [[CrossRef](#)]
42. Asgharzadeh, A.; Asgharzadeh, H.; Simchi, A. Role of grain size and oxide dispersion nanoparticles on the hot deformation behavior of AA6063: Experimental and artificial neural network modeling investigations. *Met. Mater. Int.* **2021**, *27*, 5212–5227. [[CrossRef](#)]
43. Jenab, A.; Sarraf, I.S.; Green, D.E.; Rahmaan, T.; Worswick, M.J. The use of genetic algorithm and neural network to predict rate-dependent tensile flow behaviour of AA5182-O sheets. *Mater. Des.* **2016**, *94*, 262–273. [[CrossRef](#)]
44. Yakovtseva, O.; Sitkina, M.; Mosleh, A.O.; Mikhaylovskaya, A. High strain rate superplasticity in Al-Zn-Mg-Based alloy: Microstructural design, deformation behavior, and modeling. *Materials* **2020**, *13*, 2098. [[CrossRef](#)] [[PubMed](#)]
45. Chen, W.N.; Li, S.J.; Bhandari, K.S.; Aziz, S.; Chen, X.W.; Jung, D.W. Genetic optimized Al-Mg alloy constitutive modeling and activation energy analysis. *Int. J. Mech. Sci.* **2023**, *244*, 108077. [[CrossRef](#)]
46. Yang, H.B.; Bu, H.Y.; Li, M.N.; Lu, X. Prediction of flow stress of annealed 7075 Al alloy in hot deformation using strain-compensated Arrhenius and neural network models. *Materials* **2021**, *14*, 5986. [[CrossRef](#)]
47. Quan, G.Z.; Zou, Z.Y.; Wang, T.; Liu, B.; Li, J.C. Modeling the hot deformation behaviors of as-extruded 7075 aluminum alloy by an artificial neural network with back-propagation algorithm. *High Temp. Mater. Proc.* **2016**, *36*, 1–13. [[CrossRef](#)]
48. He, D.G.; Chen, S.B.; Lin, Y.C.; Xie, H.; Li, C.B. Hot tensile behavior of a 7046-aluminum alloy: Fracture mechanisms and constitutive models. *Mater. Today Commun.* **2023**, *34*, 105209. [[CrossRef](#)]
49. Zhang, N.; Shen, S.L.; Zhou, A.N.; Jin, Y.F. Application of LSTM approach for modelling stress-strain behaviour of soil. *Appl. Soft. Comput.* **2021**, *100*, 106959. [[CrossRef](#)]
50. Kang, K.; Sun, H.B.; Zhang, C.K.; Brown, C. Short-term electrical load forecasting method based on stacked auto-encoding and GRU neural network. *Evol. Intell.* **2019**, *12*, 385–394.
51. Noh, J.; Park, H.J.; Kim, J.S.; Hwang, S.J. Gated recurrent unit with genetic algorithm for product demand forecasting in supply chain management. *Mathematics* **2020**, *8*, 565. [[CrossRef](#)]
52. Zhang, W.G.; Li, H.R.; Tang, L.B.; Gu, X.; Wang, L.Q.; Wang, L. Displacement prediction of Jiuxianping landslide using gated recurrent unit (GRU) networks. *Acta Geotech.* **2022**, *17*, 1367–1382. [[CrossRef](#)]
53. Zulqarnain, M.; Ghazali, R.; Hassim, Y.M.M.; Aamir, M. An enhanced gated recurrent unit with auto-encoder for solving text classification problems. *Arab. J. Sci. Eng.* **2021**, *46*, 8953–8967. [[CrossRef](#)]
54. Jung, S.; Moon, J.; Park, S.; Hwang, E. An attention-based multilayer GRU model for multistep-ahead short-term load forecasting. *Sensors* **2021**, *21*, 1639. [[CrossRef](#)] [[PubMed](#)]
55. Lin, Y.C.; Luo, S.C.; Jiang, X.Y.; Tang, Y.; Chen, M.S. Hot deformation behavior of a Sr-modified Al-Si-Mg alloy: Constitutive model and processing maps. *Trans. Nonferrous Met. Soc. China* **2018**, *28*, 592–603. [[CrossRef](#)]
56. Xiong, Y.B.; Wen, D.X.; Li, J.J.; Wang, K.; Zheng, Z.Z. High-temperature deformation characteristics and constitutive model of an ultrahigh strength steel. *Met. Mater. Int.* **2021**, *27*, 3945–3958. [[CrossRef](#)]
57. Yan, J.; Pan, Q.L.; Li, A.D.; Song, W.B. Flow behavior of Al-6.2Zn-0.70Mg-0.30Mn-0.17Zr alloy during hot compressive deformation based on Arrhenius and ANN models. *Trans. Nonferrous Met. Soc. China* **2017**, *27*, 638–647. [[CrossRef](#)]
58. Long, J.C.; Xia, Q.X.; Xiao, G.F.; Qin, Y.; Yuan, S. Flow characterization of magnesium alloy ZK61 during hot deformation with improved constitutive equations and using activation energy maps. *Int. J. Mech. Sci.* **2021**, *191*, 106069. [[CrossRef](#)]
59. Li, J.C.; Wu, X.D.; Liao, B.; Lin, X.M.; Cao, L.F. Simulation of low proportion of dynamic recrystallization in 7055 aluminum alloy. *Trans. Nonferrous Met. Soc. China* **2017**, *31*, 1902–1915. [[CrossRef](#)]
60. Lin, Y.C.; Chen, X.M. A critical review of experimental results and constitutive descriptions for metals and alloys in hot working. *Mater. Des.* **2011**, *32*, 1733–1759. [[CrossRef](#)]

61. Chen, M.S.; Lin, Y.C.; Ma, X.S. The kinetics of dynamic recrystallization of 42CrMo steel. *Mater. Sci. Eng. A* **2012**, *556*, 260–266. [[CrossRef](#)]
62. Tan, S.; He, D.G.; Lin, Y.C.; Zheng, B.K.; Wu, H.Y. Dislocation substructures evolution and an informer constitutive model for a Ti-55511 alloy in two-stages high-temperature forming with variant strain rates in β region. *Materials* **2023**, *16*, 3430. [[CrossRef](#)] [[PubMed](#)]

Disclaimer/Publisher’s Note: The statements, opinions and data contained in all publications are solely those of the individual author(s) and contributor(s) and not of MDPI and/or the editor(s). MDPI and/or the editor(s) disclaim responsibility for any injury to people or property resulting from any ideas, methods, instructions or products referred to in the content.